INTERNATIONAL JOURNAL FOR NUMERICAL METHODS IN FLUIDS
Int. J. Numer. Meth. Fluids 2005; **47**:19–43
Published online 28 October 2004 in Wiley InterScience (www.interscience.wiley.com). DOI: 10.1002/fld.800

A promising boundary element formulation for three-dimensional viscous flow

Xiao-Wei Gao*,†

ZONA Technology, 7430 E. Stetson Drive, Scottsdale, AZ 85251, U.S.A.

SUMMARY

In this paper, a new set of boundary-domain integral equations is derived from the continuity and momentum equations for three-dimensional viscous flows. The primary variables involved in these integral equations are velocity, traction, and pressure. The final system of equations entering the iteration procedure only involves velocities and tractions as unknowns. In the use of the continuity equation, a complex-variable technique is used to compute the divergence of velocity for internal points, while the traction-recovery method is adopted for boundary points. Although the derived equations are valid for steady, unsteady, compressible, and incompressible problems, the numerical implementation is only focused on steady incompressible flows. Two commonly cited numerical examples and one practical pipe flow problem are presented to validate the derived equations. Copyright © 2004 John Wiley & Sons, Ltd.

KEY WORDS: viscous flow; continuity equation; Navier–Stokes equations; boundary element method (BEM); domain integral

1. INTRODUCTION

The equations governing the motion of a viscous fluid are the continuity equation expressing mass conservation, and the momentum equations expressing momentum conservation. Due to the non-linearity of the convective terms appearing in the momentum equations, numerical methods must be employed to solve complicated problems. The frequently used numerical methods are the finite difference (FDM) [1], finite volume (FVM) [2] and finite element methods (FEM) [3].

The boundary element method (BEM) is a very elegant numerical method for dealing with linear problems such as potential flows, linear elasticity and viscous creeping flows (Stokes equations). The system of equations in linear BEM only involves boundary quantities and their derivatives as unknowns and therefore only the boundary of the problem needs to

*Correspondence to: X.-W. Gao, ZONA Technology, 7430 E. Stetson Drive, Scottsdale, AZ 85251, U.S.A.
†E-mail: gao@zonatech.com

Received 7 March 2004
Accepted 6 August 2004

be discretized into elements. For non-linear problems, domain integrals inevitably appear in the boundary integral equations [4] due to the lack of fundamental solutions for non-linear differential operators. As a result, the non-linear region of the domain needs to be discretized into internal cells in order to evaluate the domain integral. Nevertheless, if the non-linear region is not large, BEM is still an efficient numerical tool. Moreover, BEM is very robust in solving aerodynamics problems since the boundary conditions at infinity are automatically satisfied [5].

The first integral equation analysis for the Navier–Stokes equations in terms of vorticity and velocity was carried out by Wu and Thompson [6] through partitioning the mass and momentum conservation equations into kinematic and kinetic parts. Similar works were conducted by Skerget *et al.* [7] and Onishi *et al.* [8] using the vorticity-stream function integral approach. In order to use the successfully established BEM theory from linear elasticity, Kitagawa *et al.* [9] and Grigoriev and Fafurin [10] utilized the penalty function method to solve incompressible flow problems.

It seems that the most popular BEM formulations are those based on use of the Stokeslet fundamental solutions [11]. The first use of the Stokeslet fundamental solutions in BEM is attributed to the work by Bush and Tanner [12]. Different computation of velocity gradients appearing in the basic integral equations relates to the recent work by Aydin and Fenner [13]. To avoid the calculation of velocity gradients, Tosaka and Onishi [14] and Tosaka and Fukushima [15] integrated the domain integrals by parts to eliminate the velocity gradient term. In order to set up a boundary-only integral equation scheme, Power and Partridge [16] transformed the domain integrals of the convective terms into boundary integrals, employing the dual reciprocity method initiated by Nardini and Brebbia [17]. Further improvement to this technique refers to the works by Sarler and Kuhn [18], Power and Mingo [19] and Florez *et al.* [20].

A different type of BEM formulation was described by Dargush and Banerjee [21] for solving two-dimensional thermoviscous flow. In this formulation, a new set of fundamental solutions is used and the velocity gradient is also removed through integration by parts. A detailed description of this technique can also be found in the work by Banerjee and Honkala [22].

To date, all the existing BEM formulations described above are established for incompressible flows. Very recently, Gao [23] presented a general BEM formulation for two-dimensional viscous flow based on a reciprocal theorem in Newtonian flow. This formulation is expressed in terms of velocity, traction and pressure and is valid for steady, unsteady, compressible and incompressible flows. And more attractively, through use of the continuity equation, the pressure term can be explicitly eliminated from the final system of equations. Apart from this, since no velocity gradients appear in the integral equations, powerful existing non-linear equation solvers can be used to solve the final system and very fast convergence can be achieved.

This paper is an extension of this method to three-dimensional (3D) problems with the difference in that the basic integral equations are derived directly from the conservative form of the momentum equations rather than from the reciprocal theorem of viscous flow. Moreover, a new set of fundamental solutions for 3D problems is given and detailed formulations for evaluation of the divergence of velocity at boundary points are presented for the first time. Three examples are used to validate the correctness and efficiency of the derived formulation.

2. GOVERNING EQUATIONS IN VISCOUS FLOW

The governing equations in fluid mechanics can be derived from the conservation laws of mass, momentum, and energy [24]. In this paper, only the first two are concerned. The conservation of mass results in the *continuity* equation

$$\frac{\partial \rho}{\partial t} + \frac{\partial \rho u_k}{\partial x_k} = 0 \quad \text{or} \quad \frac{\partial \rho}{\partial t} + (\rho u_k)_{,k} = 0 \tag{1}$$

where t is time, ρ the fluid density, and u_k the kth velocity component. The repeated subscript stands for summation and $(\,)_{,k} = \partial(\,)/\partial x_k$.

The conservation of momentum gives

$$\rho \frac{\partial u_j}{\partial t} + \rho u_k u_{j,k} = \sigma_{jk,k} + \rho b_j \tag{2}$$

where b_j is the body force per unit mass (e.g. the gravity force) and σ_{jk} the stress tensor. For Newtonian fluids, the constitutive relationship between the stresses and velocities based on Stokes' hypothesis can be expressed as

$$\sigma_{jk} = -\, p\delta_{jk} + \mu(u_{j,k} + u_{k,j}) - 2\mu\delta_{jk}u_{l,l}/3 \tag{3}$$

in which p is the pressure, δ_{ij} the Kronecker delta function, and μ the viscosity (constant).

On the fluid surface with outward normal n_k, the relationship between the stress and the traction t_j (force per unit area) can be expressed as

$$t_j = \sigma_{jk} n_k \tag{4}$$

Based on these equations, a new and powerful boundary integral equation algorithm can be established.

3. BASIC INTEGRAL EQUATIONS FOR VISCOUS FLUID FLOW

Using the continuity equation (1), the momentum equation (2) can be expressed in the conservative form as

$$\frac{\partial \rho u_j}{\partial t} + (\rho u_j u_k)_{,k} = \sigma_{jk,k} + \rho b_j \tag{5}$$

Multiplying both sides of the above equation by a weight function u^*_{ij} and integrating over the domain Ω bounded with the boundary Γ, we have

$$\int_\Omega u^*_{ij} \left\{ \frac{\partial \rho u_j}{\partial t} + (\rho u_j u_k)_{,k} \right\} \mathrm{d}\Omega = \int_\Omega u^*_{ij} \{\sigma_{jk,k} + \rho b_j\} \, \mathrm{d}\Omega \tag{6}$$

Integrating equation (6) by parts and using divergence theorem, it follows that

$$\int_\Omega u_{ij}^* \frac{\partial \rho u_j}{\partial t}\,\mathrm{d}\Omega + \int_\Gamma u_{ij}^* \rho u_j u_k n_k\,\mathrm{d}\Gamma - \int_\Omega u_{ij,k}^* \rho u_j u_k\,\mathrm{d}\Omega$$
$$= \int_\Gamma u_{ij}^* \sigma_{jk} n_k\,\mathrm{d}\Gamma - \int_\Omega u_{ij,k}^* \sigma_{jk}\,\mathrm{d}\Omega + \int_\Omega u_{ij}^* \rho b_j\,\mathrm{d}\Omega \tag{7}$$

Substituting Equation (3) into the second integral on the right-hand side of the above equation and repeating the application of the divergence theorem and integration by parts, we can obtain

$$\int_\Omega u_{ij,k}^* \sigma_{jk}\,\mathrm{d}\Omega = -\int_\Omega u_{ij,j}^* p\,\mathrm{d}\Omega + \int_\Gamma t_{ij}^* u_j\,\mathrm{d}\Gamma - \int_\Omega \mu(u_{ij,kk}^* + u_{ik,kj}^*/3)\,u_j\,\mathrm{d}\Omega \tag{8}$$

where

$$t_{ij}^* = \mu(u_{ij,k}^* + u_{ik,j}^* - \delta_{jk} u_{il,l}^* 2/3) n_k \tag{9}$$

Now we choose the weight function u_{ij}^* to be the fundamental solutions of the following equations:

$$\mu(u_{ij,kk}^* + u_{ik,kj}^*/3) + \delta(y-x)\delta_{ij} = 0 \tag{10}$$

where $\delta(y-x)$ is the Dirac delta function of y at point x.

The fundamental solutions of Equation (10) for 3D problems can be derived as

$$u_{ij}^*(x,y) = \frac{1}{32\pi\mu r}\{7\delta_{ij} + r_{,i}\, r_{,j}\} \tag{11}$$

where r is the distance between points x and y, and a particular notation is made here that is $r_{,i} = \partial r/\partial y_i = (y_i - x_i)/r$.

Now substituting Equation (10) into the last integral of Equation (8) yields

$$\int_\Omega u_{ij,k}^* \sigma_{jk}\,\mathrm{d}\Omega = -\int_\Omega u_{ij,j}^* p\,\mathrm{d}\Omega + \int_\Gamma t_{ij}^* u_j\,\mathrm{d}\Gamma + u_i(x) \tag{12}$$

in which t_{ij}^* can be expressed by substituting Equation (11) into (9) as

$$t_{ij}^*(x,y) = \frac{-3}{16\pi r^2}\{n_i r_{,j} - n_j r_{,i} + (r_{,i}\, r_{,j} + \delta_{ij}) n_k r_{,k}\} \tag{13}$$

Finally, substituting Equation (12) into Equation (7) and taking into account Equation (4), we obtain

$$u_i(x) = \int_\Gamma u_{ij}^*(x,y) t_j(y)\,\mathrm{d}\Gamma(y) - \int_\Gamma t_{ij}^*(x,y) u_j(y)\,\mathrm{d}\Gamma(y)$$
$$- \int_\Gamma u_{ij}^*(x,y) n_k(y) \rho(y) u_j(y) u_k(y)\,\mathrm{d}\Gamma(y)$$

$$+\int_\Omega u^*_{ij,k}(x,y)\rho(y)u_j(y)u_k(y)\,\mathrm{d}\Omega(y)$$

$$+\int_\Omega u^*_{ij}(x,y)\rho(y)b_j(y)\,\mathrm{d}\Omega(y)-\int_\Omega u^*_{ij}(x,y)\frac{\partial \rho u_j}{\partial t}\,\mathrm{d}\Omega(y)$$

$$+\int_\Omega u^*_{ij,j}(x,y)\,p(y)\,\mathrm{d}\Omega(y) \tag{14}$$

where

$$u^*_{ij,k}(x,y)=\frac{-1}{32\pi\mu r^2}\{7\delta_{ij}r_{,k}-\delta_{ik}r_{,j}-\delta_{jk}r_{,i}+3\,r_{,i}\,r_{,j}\,r_{,k}\} \tag{15}$$

$$u^*_{ij,j}=\frac{-3r_{,i}}{16\pi\mu r^2} \tag{16}$$

Equation (14) is a general boundary integral equation valid for steady, unsteady, compressible, and incompressible flows. From the kernel function $t^*_{ij}(x,y)$ in Equation (13), we can see that the second integral in Equation (14) is strongly singular when the source point (collocation point) x approaches the field point y. Therefore, Equation (14) is only bounded for internal collocation points. Fortunately, the rigid body motion strategy can be used to handle this integral for boundary collocation points. The procedure is exactly the same as in the conventional BEM [25]. It is not repeated here. Except for the second integral, all other integrals in Equation (14) are weakly singular and therefore can be evaluated accurately by using the element/cell sub-division technique [25].

In Equation (14), pressure p appears in the domain integral and therefore one more equation is needed for this unknown. In addition, the velocity/traction–pressure coupled equation set may result from Equation (14). In the next section, one more equation will be provided based on the continuity equation and the pressure can explicitly be expressed in terms of velocities and tractions.

4. PRESSURE EQUATIONS BASED ON CONTINUITY EQUATION

The continuity equation (1) can be written as

$$\frac{\partial \rho}{\partial t}+u_i\frac{\partial \rho}{\partial x_i}+\rho\frac{\partial u_i}{\partial x_i}=0 \tag{17}$$

In order to use this equation, the divergence of velocity, $\partial u_i/\partial x_i$, needs to be determined. For internal points, it can be obtained by directly differentiating the basic integral equation (14). However, for points located on the boundary of the problem, directly differentiating Equation (14) results in a hyper-singular boundary integral and consequently gives rise to a difficulty in numerical computation. In this paper, the traction-recovery method will be used for boundary points.

4.1. Pressure equations for internal points

Differentiating Equation (14) with respect to the source point x yields

$$\begin{aligned}\frac{\partial u_i(x)}{\partial x_i} = &\int_\Gamma \frac{\partial u^*_{ij}(x,y)}{\partial x_i} t_j(y)\,\mathrm{d}\Gamma(y) - \int_\Gamma \frac{\partial t^*_{ij}(x,y)}{\partial x_i} u_j(y)\,\mathrm{d}\Gamma(y)\\ &- \int_\Gamma \frac{\partial u^*_{ij}(x,y)}{\partial x_i} n_k(y)\rho(y)u_j(y)u_k(y)\,\mathrm{d}\Gamma(y)\\ &+ \int_\Omega \frac{\partial u^*_{ij,k}(x,y)}{\partial x_i}\rho(y)u_j(y)u_k(y)\,\mathrm{d}\Omega(y)\\ &+ \int_\Omega \frac{\partial u^*_{ij}(x,y)}{\partial x_i}\rho(y)b_j(y)\,\mathrm{d}\Omega(y) - \int_\Omega \frac{\partial u^*_{ij}(x,y)}{\partial x_i}\frac{\partial \rho u_j}{\partial t}\,\mathrm{d}\Omega(y)\\ &+ \int_\Omega \frac{\partial u^*_{ij,j}(x,y)}{\partial x_i} p(y)\,\mathrm{d}\Omega(y) \end{aligned} \tag{18}$$

Let's first handle the last domain integral of Equation (18). Cutting a small spherical domain Ω_ε with radius ε centred at point x from domain Ω (Figure 1) and noticing that $\partial(\,)/\partial x_i = -\partial(\,)/\partial y_i = -(\,)_{,i}$, we have

$$\begin{aligned}\int_\Omega \frac{\partial u^*_{ij,j}(x,y)}{\partial x_i} p(y)\,\mathrm{d}\Omega(y) &= -\lim_{\varepsilon\to 0}\int_{\Omega-\Omega_\varepsilon} u^*_{ij,ji}(x,y)\,p(y)\,\mathrm{d}\Omega(y) - p(x)\lim_{\varepsilon\to 0}\int_{\Omega_\varepsilon}\frac{\partial u^*_{ij,j}(x,y)}{\partial y_i}\,\mathrm{d}\Omega(y)\\ &= -\int_\Omega u^*_{ij,ji}(x,y)\,p(y)\,\mathrm{d}\Omega(y) - p(x)\lim_{\varepsilon\to 0}\int_{\Gamma_\varepsilon} u^*_{ij,j}(x,y)n_i\,\mathrm{d}\Gamma(y)\end{aligned}$$

where Γ_ε is the spherical surface of the domain Ω_ε. By differentiating Equation (16), we can find that $u^*_{ij,ji}(x,y) = 0$. So the first integral on the right-hand side of the above equation

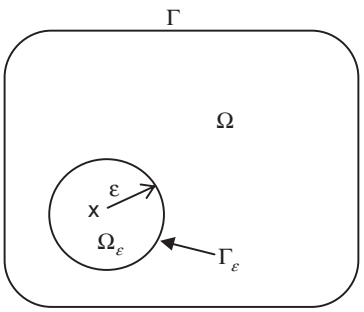

Figure 1. A small domain Ω_ε cut out from Ω.

disappears and the second one can be easily integrated such that

$$\int_{\Omega} \frac{\partial u^*_{ij,j}(x,y)}{\partial x_i}\, p(y)\, \mathrm{d}\Omega(y) = \frac{3}{4\mu}\, p(x) \tag{19}$$

Close inspection of other domain integrals in Equation (18) reveals that after direct differentiation, the kernel $\partial u^*_{ij,k}(x,y)/\partial x_i$ will become strongly singular. This makes the corresponding domain integral unbounded. To avoid this, the complex-variable method (CVM) introduced in BEM by Gao *et al.* [26] is adopted to evaluate the derivatives of all kernels appearing in Equation (18). Using CVM, the order of singularities can be reduced by one.

In CVM, the variable x of a real function $f(x)$ is replaced by a complex one, $x + Ih$ with h being the step size. The derivative of the above equation can be expressed [26] as:

$$\frac{\mathrm{d}f}{\mathrm{d}x} = \frac{\mathrm{Im}(f(x+Ih))}{h} \tag{20}$$

where the symbol 'Im' denotes the imaginary part. In numerical implementation, the step-size h is usually set to 10^{-20}, so that the result is step-size independent. As an example, let's consider the function $f(x,y,z) = x^2 y + xz$. Apparently, $\partial f(x,y,z)/\partial x = 2xy + z$. If using CVD, it follows that

$$f(x+Ih, y, z) = (x+Ih)^2 y + (x+Ih)z = [(x^2 - h^2)y + xz] + h(2xy + z)I$$

The imaginary part of this expression is $\mathrm{Im}(f(x+Ih, y, z)) = h(2xy+z)$ and immediately we obtain that

$$\frac{\mathrm{Im}(f(x+I\,h, y, z))}{h} = 2xy + z$$

This is exactly the same as the analytical solution.

CVM can be easily used to evaluate the derivatives appearing in Equation (18). Let's consider the co-ordinates at the source point x as complex variables by adding a small imaginary part Ih to the ith co-ordinate. According to Equation (20) and accounting for Equation (19), it follows from Equations (17) and (18) that

$$\begin{aligned} p(x) = &- \int_{\Gamma} u'^*_j(x,y) t_j(y)\, \mathrm{d}\Gamma(y) + \int_{\Gamma} t'^*_j(x,y) u_j(y)\, \mathrm{d}\Gamma(y) \\ &+ \int_{\Gamma} u'^*_j(x,y) n_k(y) \rho(y) u_j(y) u_k(y)\, \mathrm{d}\Gamma(y) \\ &- \int_{\Omega} u'^*_{j,k}(x,y) \rho(y) u_j(y) u_k(y)\, \mathrm{d}\Omega(y) \\ &- \int_{\Omega} u'^*_j(x,y) \rho(y) b_j(y)\, \mathrm{d}\Omega(y) + \int_{\Omega} u'^*_j(x,y) \frac{\partial \rho u_j}{\partial t}\, \mathrm{d}\Omega(y) \\ &- \frac{4\mu}{3\rho}\left(u_i \frac{\partial \rho}{\partial x_i} + \frac{\partial \rho}{\partial t}\right) \end{aligned} \tag{21}$$

where

$$u_j'^*(x,y) = \frac{4\mu}{3h}\,\mathrm{Im}(u_{ij}^*(x_i + Ih, y))$$

$$t_j'^*(x,y) = \frac{4\mu}{3h}\,\mathrm{Im}(t_{ij}^*(x_i + Ih, y)) \tag{22}$$

$$u_{j,k}'^*(x,y) = \frac{4\mu}{3h}\,\mathrm{Im}(u_{ij,k}^*(x_i + Ih, y))$$

Comparison of Equation (21) with Equation (14) reveals that the singularities involved in the expression of the divergence of the velocity are the same as those occurring in the velocity integral equation (14). Therefore, every integral in Equation (21) can be evaluated accurately.

Equation (21) can only be applied to internal points. For boundary points, the kernel $t_j'^*$ is still singular even using CVM, so the traction-recovery method is used in this paper.

4.2. *Pressure equations for boundary points*

For a boundary point x, a local Cartesian co-ordinate system x_I' is defined, in which the axes x_1' and x_2' are tangential to the boundary surface and x_3' is directed in the normal direction (Figure 2).

The velocity and traction along the normal direction can be expressed as

$$u_n = u_i n_i$$
$$t_n = t_i n_i \tag{23}$$

and derivatives along the normal direction are calculated by

$$\frac{\partial}{\partial n} = n_i \frac{\partial}{\partial x_i} \tag{24}$$

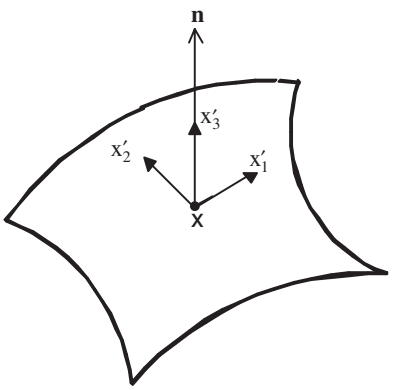

Figure 2. Local orthogonal set of axes over boundary surface.

With relationships (23) and (24) in mind, substituting Equation (3) into Equation (4) and multiplying both sides with n_j, it follows that

$$t_n = -p + 2\mu \frac{\partial u_n}{\partial n} - \frac{2\mu}{3} \frac{\partial u_i}{\partial x_i} \tag{25}$$

Noticing that the quantity, $\partial u_i/\partial x_i$, is independent of orthogonal co-ordinate systems, the divergence of velocity can be expressed in the local co-ordinate system as

$$\frac{\partial u_i}{\partial x_i} = \frac{\partial u_n}{\partial n} + \varepsilon_\tau \tag{26}$$

where

$$\varepsilon_\tau = \frac{\partial u_1'}{\partial x_1'} + \frac{\partial u_2'}{\partial x_2'} = \frac{\partial u_I'}{\partial x_I'} \quad (I = 1, 2) \tag{27}$$

In Equation (27), u_1' and u_2' are tangential components of velocity which, along with the local co-ordinates, are related to global values by

$$\begin{aligned} u_I' &= L_{Ij} u_j \\ x_I' &= L_{Ij} x_j \end{aligned} \tag{28}$$

where L_{Ij} $(I = 1, 2;\ j = 1, 2, 3)$ are the direction cosines of the axes x_1' and x_2'. The determination of L_{Ij} and n_i can be found in references (e.g. Reference [25]).

To determine $\partial u_I'/\partial x_I'$ explicitly in Equation (27), we need to use shape functions $N_\alpha(\xi, \eta)$ defined for a boundary element including point x. The velocity and co-ordinates at point x with the intrinsic co-ordinates (ξ, η) can be expressed as

$$\begin{aligned} u_j &= \sum_\alpha N_\alpha(\xi, \eta) u_j^\alpha \\ x_j &= \sum_\alpha N_\alpha(\xi, \eta) x_j^\alpha \end{aligned} \tag{29}$$

where u_j^α and x_j^α are the jth components of the velocity and co-ordinates at node α, respectively. The shape functions $N_\alpha(\xi, \eta)$ can be found in BEM and FEM books [25].

Using Equations (28) and (29), we have

$$\varepsilon_\tau = \frac{\partial u_I'}{\partial x_I'} = \frac{\partial u_I'}{\partial \xi} \frac{\partial \xi}{\partial x_I'} + \frac{\partial u_I'}{\partial \eta} \frac{\partial \eta}{\partial x_I'} = L_{Ij} \sum_\alpha u_j^\alpha \left(\frac{\partial N_\alpha(\xi, \eta)}{\partial \xi} \frac{\partial \xi}{\partial x_I'} + \frac{\partial N_\alpha(\xi, \eta)}{\partial \eta} \frac{\partial \eta}{\partial x_I'} \right) \tag{30}$$

where $\partial \xi/\partial x_I'$ and $\partial \eta/\partial x_I'$ can be computed using the following matrix equation:

$$\begin{bmatrix} \dfrac{\partial \xi}{\partial x_1'} & \dfrac{\partial \xi}{\partial x_2'} \\ \dfrac{\partial \eta}{\partial x_1'} & \dfrac{\partial \eta}{\partial x_2'} \end{bmatrix} = \begin{bmatrix} \dfrac{\partial x_1'}{\partial \xi} & \dfrac{\partial x_1'}{\partial \eta} \\ \dfrac{\partial x_2'}{\partial \xi} & \dfrac{\partial x_2'}{\partial \eta} \end{bmatrix}^{-1} \tag{31}$$

where

$$\frac{\partial x_I'}{\partial \xi} = L_{Ij} \sum_{\alpha} x_j^{\alpha} \frac{\partial N_{\alpha}(\xi, \eta)}{\partial \xi}$$
$$\frac{\partial x_I'}{\partial \eta} = L_{Ij} \sum_{\alpha} x_j^{\alpha} \frac{\partial N_{\alpha}(\xi, \eta)}{\partial \eta} \tag{32}$$

Now that the quantity ε_τ is determined by Equation (30), the continuity equation (17) can be written by using Equation (26) as

$$\rho \frac{\partial u_n}{\partial n} = -\rho \varepsilon_\tau - u_i \frac{\partial \rho}{\partial x_i} - \frac{\partial \rho}{\partial t} \tag{33}$$

Finally, substituting Equations (33) and (26) into Equation (25), we obtain

$$p = -t_n - 2\mu \varepsilon_\tau - \frac{4\mu}{3\rho} \left(u_i \frac{\partial \rho}{\partial x_i} + \frac{\partial \rho}{\partial t} \right) \tag{34}$$

From this equation it can be seen that in general the pressure p is not equal to the normal surface force t_n in value even for a steady incompressive viscous flow. The tangential strain rate ε_τ also has a contribution to the pressure value. This phenomenon will be clarified in numerical example 6.3.

Equations (34) and (21) are used to close the equation set provided by Equation (14) for problems with unknowns being velocity/traction and pressure in incompressible flows. For compressive flows, the density ρ is also unknown. In this case, the energy equation and equation of state are required to close the final system of equations. This will be described in another paper.

As will be seen in the next section, Equations (34) and (21) enable us to eliminate the pressure term from the final system of equations.

5. NUMERICAL IMPLEMENTATION FORMULATIONS FOR STEADY INCOMPRESSIBLE FLOWS

Equations (14), (21), and (34) are applicable to general viscous flows. In this section, the detailed numerical implementation of these equations in steady incompressible flows is described. In this case, the following equations should be applied to Equations (14), (21), and (34):

$$\frac{\partial \rho}{\partial x_i} = 0, \quad \frac{\partial \rho}{\partial t} = 0, \quad \frac{\partial \rho u_j}{\partial t} = 0 \tag{35}$$

Numerical implementation of Equations (14), (21), and (34) requires discretization of the boundary Γ into boundary elements and the domain Ω into internal cells. As in Equation (29), for each boundary element or internal cell, the velocity, traction and pressure can be

expressed in terms of their nodal values through shape functions as follows:

$$u_j = \sum_{\alpha} N_\alpha u_j^\alpha \tag{36}$$

$$t_j = \sum_{\alpha} N_\alpha t_j^\alpha \tag{37}$$

$$p = \sum_{\alpha} N_\alpha p^\alpha \tag{38}$$

where N_α are shape functions for boundary elements and internal cells [25], p^α represents the value of pressure p at node α. For the sake of simplicity to assemble, the non-linear term $u_j u_k$ is approximated using the following equation:

$$u_j u_k = \sum_{\alpha} N_\alpha u_j^\alpha u_k^\alpha \tag{39}$$

Substituting Equations (35)–(39) into the discretized form of the integral equation (14) and collocating x for all boundary nodes (rigid body motion is used for determination of diagonal terms) yields the following algebraic matrix equation:

$$[H]\{u\} = [G]\{t\} + \{b\} + [C_b]\{p\} + [D_b]\{u^2\} \tag{40}$$

where $\{u\}$ and $\{t\}$ are vectors consisting of velocities and tractions at all boundary nodes, respectively, and $\{b\}$ is a constant vector associated with body forces. And $\{p\}$ and $\{u^2\}$ are vectors consisting of pressure and velocity products at all nodes (i.e. boundary and internal nodes). The latter can be clearly shown as

$$\{u^2\} = \{(u_1^1)^2, u_1^1 u_2^1, u_1^1 u_3^1, (u_2^1)^2, u_2^1 u_3^1, (u_3^1)^2, \ldots, (u_1^n)^2, u_1^n u_2^n, u_1^n u_3^n, (u_2^n)^2, u_2^n u_3^n, (u_3^n)^2\}^{\mathrm{T}} \tag{41}$$

in which n is the total number of all nodes.

In each direction of a boundary node, either velocity or traction is specified as a boundary condition. So after applying boundary conditions to Equation (40) and rearranging the equation, it follows that

$$[A_b]\{X\} = \{Y_b\} + [C_b]\{p\} + [D_b]\{u^2\} \tag{42}$$

where $\{X\}$ is a vector consisting of unknown velocities and unknown tractions, and $\{Y_b\}$ is a known vector.

Similarly, for internal nodes, Equation (14) gives

$$\{u_I\} = [A_I]\{X\} + \{Y_I\} + [C_I]\{p\} + [D_I]\{u^2\} \tag{43}$$

where $\{u_I\}$ is a vector consisting of all velocities at internal nodes. Finally, from Equations (21) and (34) we have

$$\{p\} = [A_p]\{X\} + \{Y_p\} + [D_p]\{u^2\} \tag{44}$$

It is noted that in Equation (44), the matrix $[D_p]$ has zero value at the position of boundary nodes.

Manipulating the set of equations (42)–(44), we obtain

$$\{X\} = \{Y^x\} + [D^x]\{u^2\} \tag{45}$$

$$\{u^I\} = \{Y^I\} + [D^I]\{u^2\} \tag{46}$$

$$\{p\} = \{Y^p\} + [D^p]\{u^2\} \tag{47}$$

where

$$\begin{aligned} \{Y^x\} &= [A]^{-1}(\{Y_b\} + [C_b]\{Y_p\}) \\ \{D^x\} &= [A]^{-1}([D_b] + [C_b][D_p]) \\ [A] &= [A_b] - [C_b][A_p] \end{aligned} \tag{48}$$

$$\begin{aligned} \{Y^p\} &= \{Y_p\} + [A_p]\{Y^x\} \\ [D^p] &= [D_p] + [A_p][D^x] \end{aligned} \tag{49}$$

$$\begin{aligned} \{Y^I\} &= \{Y_I\} + [A_I]\{Y^x\} + [C_I]\{Y^p\} \\ [D^I] &= [D_I] + [A_I][D^x] + [C_I][D^p] \end{aligned} \tag{50}$$

Equations (45)–(47) constitute the final system of equations with $\{X\}$ and $\{u^I\}$ as unknowns. For the cases of very slowly flowing fluids (Stokes flow problems), the terms related to $\{u^2\}$ are very small compared with other terms and thus may be neglected. In these cases, the solutions of problem are directly given by $\{Y^x\}$, $\{Y^I\}$ and $\{Y^p\}$. However, for general cases, the terms associated with $\{u^2\}$ are not small and are non-linear in velocity. Therefore, an iterative process is needed to solve the equation set (45)–(47). Among these three equations, only Equations (45) and (46) are needed in the iterative solving process. Once the iteration converges, the values of velocities are plugged in Equation (47) to compute pressures.

In the assembling process of the above system of equations, it can be seen that the inverse of matrix $[A]$ is needed in Equation (48). The order of matrix $[A]$ is three times that of the number of boundary nodes. For problems with a moderate number of surface nodes, inverting matrix $[A]$ takes little time. However, for problems with a huge number of surface nodes, this process takes considerable computational time. In this case, using a powerful matrix inverse tool is important, although the *Gauss–Jordan elimination* method is used in this study.

The advantage of this representation of the system of equations over the existing 'pseudo-body force' representations is that the velocities explicitly appear in the system of equations. Therefore, the first and second derivatives of the system with respect to velocities can easily be derived so that any advanced non-linear equation solver can be applied to solve the system of equations. In this paper, the program HYBRJ [27] using the *modified Powell hybrid algorithm* is adopted to solve the equation set (45) and (46).

6. NUMERICAL EXAMPLES

Three numerical examples of steady incompressible viscous flows are presented to demonstrate the correctness and potential of the theory presented in this paper. The first two are well-known two-dimensional flows which have analytical and benchmark solutions to verify. They are simulated using 3D models. The third one is a truly 3D pipe flow subjected to a body force. All these examples were computed on a PC computer (2 GHz, 256 Mb RAM).

6.1. Poiseuille flow

In order to validate the formulations derived in this paper, the simplest Poiseuille flow is considered first. The fluid flows between two flat plates under constant pressure gradient without body forces (Figure 3). For this simple problem, analytical solutions are available [28]. The horizontal velocity can be expressed as

$$u_x = -\frac{p'}{2\mu} z(H - z)$$

where $H = 1$ is the distance between upper and lower surfaces, $p' = \mathrm{d}p/\mathrm{d}x = 10$ is the gradient of pressure.

To model this problem, a rectangular prism is used for BEM mesh (Figure 4), which is discretized into 1144 equally spaced four-noded boundary elements with 1146 boundary nodes

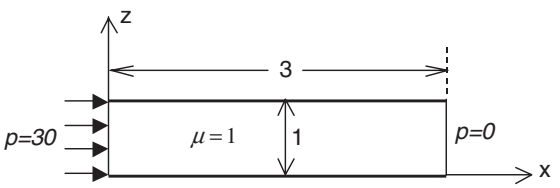

Figure 3. Geometry and boundary condition for Poiseuille flow in x–z plane.

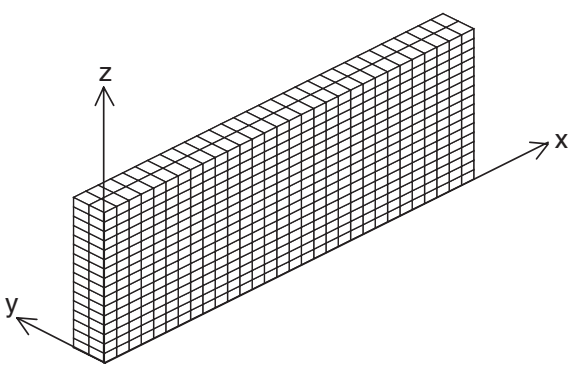

Figure 4. BEM model of Poiseuille flow.

Table I. Horizontal velocities along z direction.

z	0.125	0.25	0.375	0.5	0.625	0.75	0.875
Current	0.548854	0.94032	1.175236	1.253541	1.175237	0.940322	0.548857
Exact	0.54687	0.9375	1.17187	1.25	1.171875	0.9375	0.546875

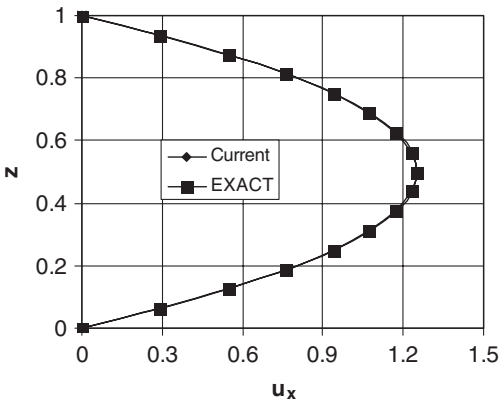

Figure 5. Velocity profile along vertical direction.

and 960 eight-noded internal cells with 435 internal nodes. The 'no-slip' condition is applied to upper and lower surfaces and the 'slip' condition to front and back surfaces. The boundary conditions on left and right surfaces can be expressed as

$$\left.\begin{aligned} t_x &= p = 30, \\ u_y &= u_z = 0, \end{aligned}\right\} \quad \text{on surface } x = 0$$

$$\left.\begin{aligned} t_x &= p = 0, \\ u_y &= u_z = 0, \end{aligned}\right\} \quad \text{on surface } x = 3$$

Table I lists the computed horizontal velocities and analytical solutions along z direction at middle section. Figure 5 plots the profile of the horizontal velocity. Since this problem is density-independent, only two iterations are needed to reach the convergence tolerance of 10^{-8}.

From Figure 5, we can see that the results from the current method are in good agreement with the exact solutions.

6.2. *Driven flow in an unitary square cavity*

The second numerical example concerned is a unitary square cavity (Figure 6). The top surface moves with a uniform velocity of 1 in the horizontal direction, while the left, right and bottom surfaces are fixed, including the four corners of the top surface. The front and back surfaces are applied by 'slip' condition. Ghia *et al.* [29] provided a benchmark solution that is commonly cited for comparison purposes (e.g. References [13, 30]).

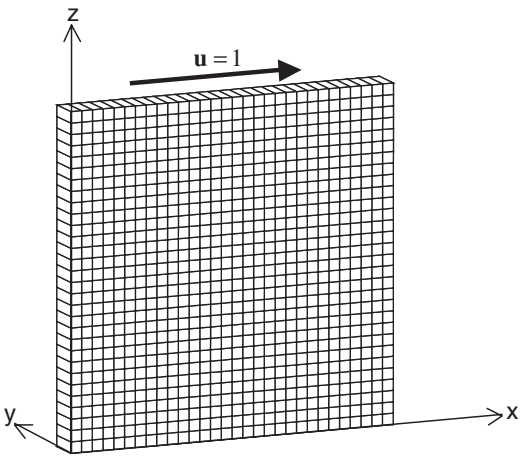

Figure 6. BEM model for driven cavity flow.

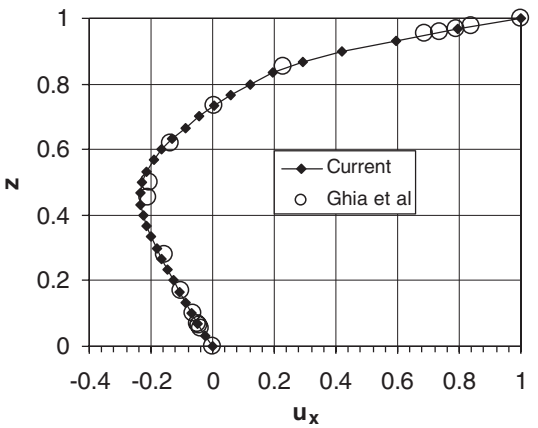

Figure 7. Horizontal velocity profile on vertical centre surface of the driven cavity.

The problem is discretized into 60 equally spaced linear boundary elements along x and z directions and 1 element along y direction, with a total of 1920 boundary elements and 900 linear cells and 1922 boundary nodes. For this model, no internal nodes exist.

The Reynolds number is defined as $Re = \rho UH/\mu$, where U is the characteristic velocity and H the characteristic length. In this example, the parameters are set as $\rho = 100$, $U = 1$, $H = 1$, and $\mu = 1$. This implies that $Re = 100$. Figure 7 shows the computed horizontal velocities on the vertical centre surface of the cavity and Figure 8 depicts the vertical velocity profile on the horizontal centre surface. The traction distribution over the top surface of the cavity is plotted in Figure 9. Figure 10 gives the velocity vector plot. The computed vortex centre is $(0.6102, 0.7362)$, which is close to the result $(0.6172, 0.7344)$ by Ghia *et al.* [29]. The iteration history is shown in Figure 11 for the given convergence tolerance of 10^{-8}. The convergence is achieved after 31 iterations.

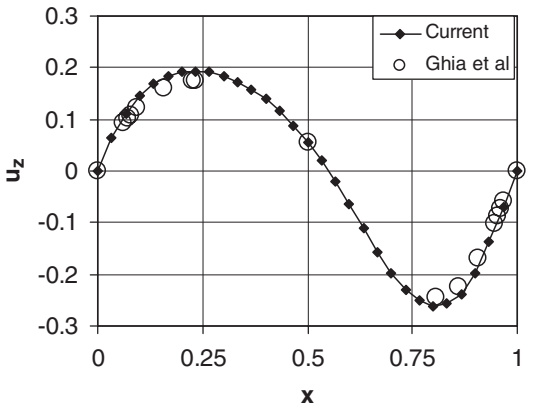

Figure 8. Vertical velocity profile on horizontal centre surface of the driven cavity.

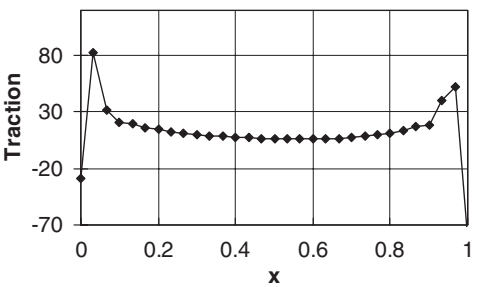

Figure 9. Traction distribution along top surface.

Comparison of the current results with the benchmark solutions in Figures 7 and 8 indicates that the method described in this paper is correct and the iteration history in Figure 11 shows that fast convergence can be achieved using the current method.

6.3. *Curved pipe flow*

The third example deals with the fluid flowing through a 3D curved circular pipe with radius $r = 1$ (Figure 12). The curvature of the pipe is determined by a radius of $R = 9$. The fluid with the property of $\mu = 1$ and $\rho = 1$ is subjected to a vertical body force of $b_z = 10$ and a pressure P on the top surface. The discretized BEM model of this problem is shown in Figure 13. Due to symmetry about the x–z plane, only half of the model is used in computation. The discretized half pipe consists of 672 linear boundary elements with 719 boundary nodes and 2880 linear cells with 2784 internal nodes. Three different sets of boundary conditions applying to the two end surfaces are considered (Table II). The first condition (B.C.1) is the traction boundary condition. The second (B.C.2) is the velocity/traction mixing boundary condition, that is, the tangential velocity is constrained and normal traction is specified. The

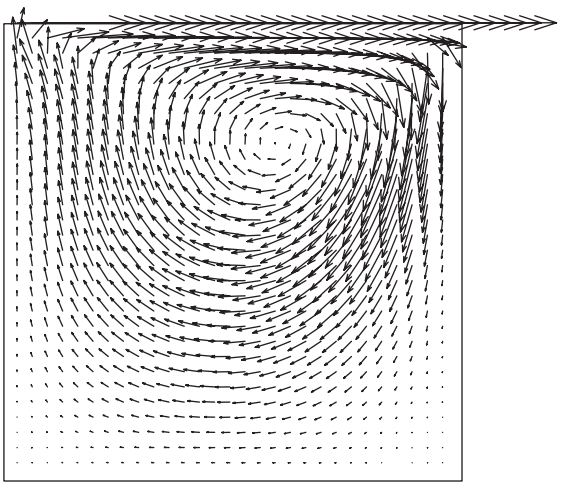

Figure 10. Velocity vectors in the x–z plane.

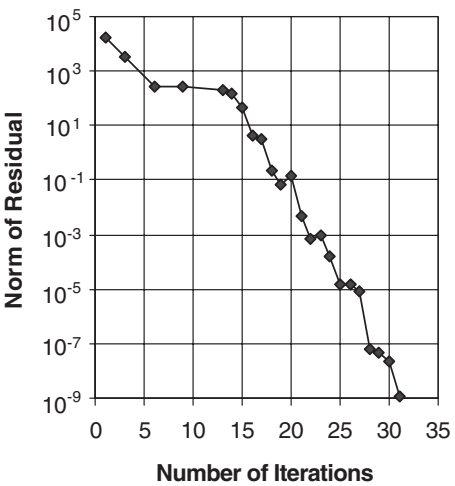

Figure 11. Iteration history for driven cavity flow.

third set of boundary conditions (B.C.3) is the free boundary condition (applied traction being zero) and only the body force is imposed through the domain.

Figure 14 is the computed velocity vector plot for different cross-sections over the vertical central plane $y = 0$ using B.C.1, where the velocity vector is scaled by multiplying with a factor of 0.2. Figure 15 is the plot without scaling. Table III lists the results at positions of maximum velocity over the different sections numbered in Figure 14. Figure 16 is the contour plot of pressure over the vertical central plane. The results for B.C.2 and B.C.3 are shown in Figures 17 and 18 and Tables IV and V. Since the velocity vector plots for B.C.2

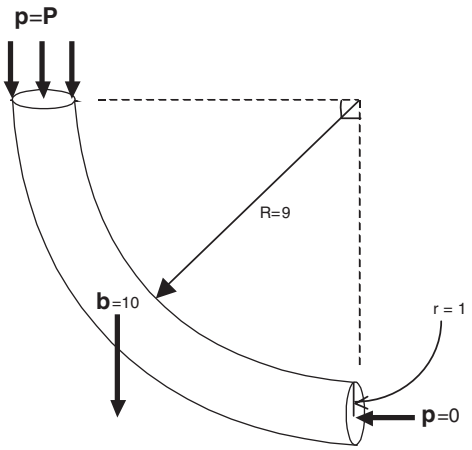

Figure 12. Flow through a curved pipe.

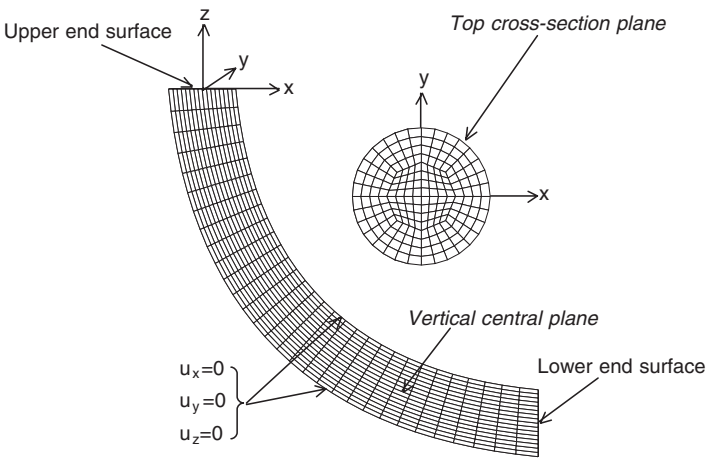

Figure 13. BEM model of the curved pipe.

Table II. Three sets of boundary conditions specified on two end surfaces.

	Upper end surface	Lower end surface	Remarks
B.C.1	$t_x = t_y = 0,\ t_z = -50$	$t_x = t_y = t_z = 0$	Traction condition
B.C.2	$u_x = u_y = 0,\ t_z = -50$	$u_y = u_z = 0,\ t_x = 0$	Mixing condition
B.C.3	$t_x = t_y = t_z = 0$	$t_x = t_y = t_z = 0$	Body force only

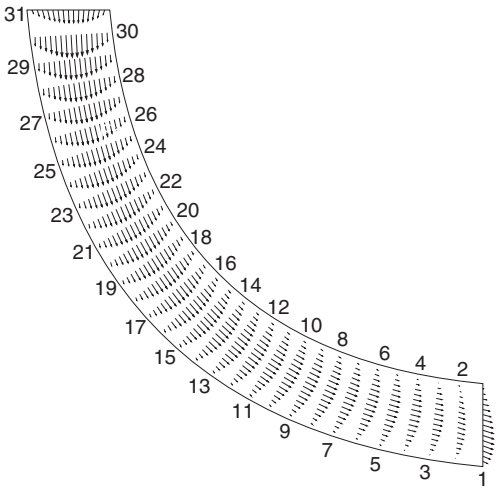

Figure 14. Scaled velocity vector plot for different sections over vertical central plane using traction boundary condition (B.C.1).

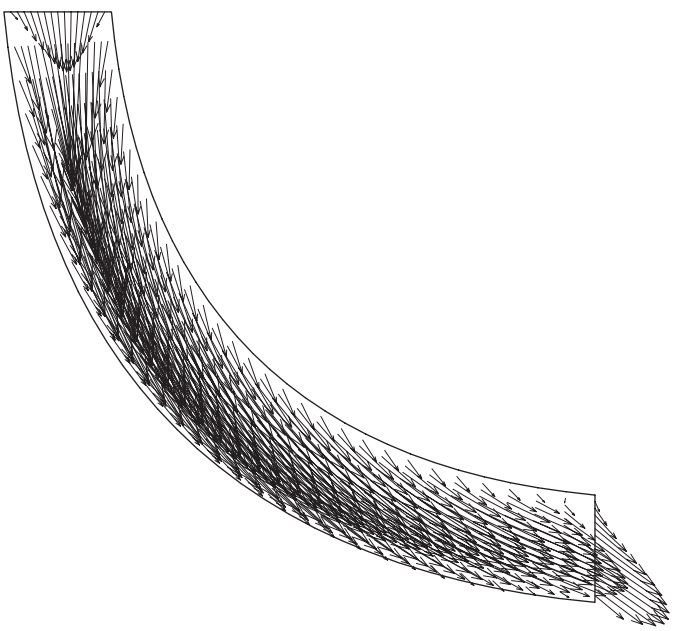

Figure 15. Full velocity vector plot for different sections over vertical central plane using traction boundary condition (B.C.1).

and B.C.3 are similar to those from B.C.1, they are not plotted here. The iteration history is shown in Figure 19 for B.C.1 for the given convergence tolerance of 10^{-8}. The convergence is achieved after 16 iterations.

Table III. Results at maximum velocity position of each section over the vertical central plane $y=0$ (see Figure 14) using traction boundary condition (B.C.1).

Section	x	z	u_x	u_z	$\|u\|$	p
1	10.000	−10.250	1.9593	−0.6504	2.0644	−1.6262
3	8.8179	−9.8488	1.5734	−0.3890	1.6208	9.1021
5	7.7094	−9.6240	1.7870	−0.5257	1.8627	16.0389
7	6.6745	−9.3255	1.8425	−0.7386	1.9851	22.1204
9	5.7133	−8.9534	1.8423	−0.9610	2.0778	27.2860
11	4.8257	−8.5076	1.8029	−1.1930	2.1619	31.5646
13	4.0118	−7.9882	1.7290	−1.4325	2.2453	35.0271
15	3.2715	−7.3952	1.6234	−1.6750	2.3326	37.7730
17	2.6048	−6.7285	1.4890	−1.9151	2.4259	39.9218
19	2.0118	−5.9882	1.3305	−2.1477	2.5265	41.6027
21	1.4924	−5.1743	1.1538	−2.3712	2.6370	42.9407
23	1.0466	−4.2867	0.9659	−2.5867	2.7611	44.0433
25	0.6745	−3.3255	0.7752	−2.8086	2.9137	44.9647
27	0.3760	−2.2906	0.5868	−3.0871	3.1424	45.6331
29	0.1512	−1.1821	0.3579	−3.6088	3.6265	45.5448
31	0.1250	0.0000	0.0289	−2.3579	2.3581	53.1565

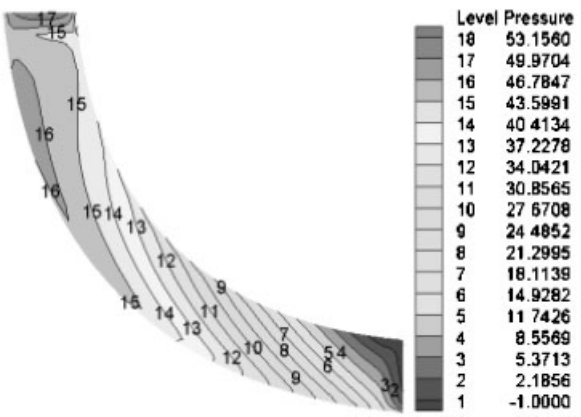

Figure 16. Contour plot of pressure over the vertical central plane using traction boundary condition (B.C.1).

From Tables III and V, it can be seen that the pressure of section 31 is not equal to the applied normal force $P=50$. This is because the tangential velocities u_x and u_y are not zero and therefore the resulting tangential strain rate ε_τ has a contribution to the pressure (see Equation (34)). However, this phenomenon does not occur in the case of B.C.2, where the tangential velocity is constrained and thus the pressure of section 31 is exactly the value of the applied normal force $P=50$. It is interesting to note that the maximum pressure in the body force case (B.C.3) occurs in the middle part of the tube rather than on the top of the tube as in the cases of B.C.1 and B.C.2.

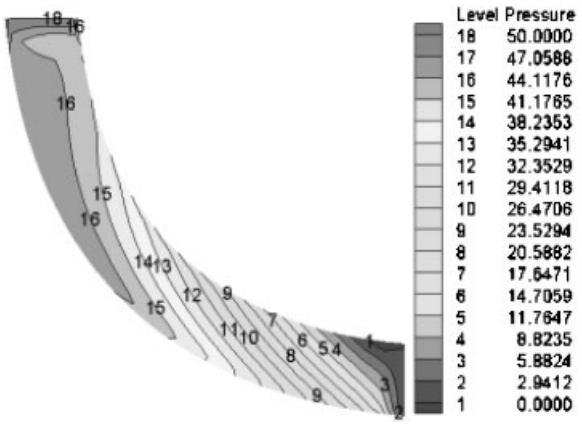

Figure 17. Contour plot of pressure over the vertical central plane using tangential velocity and normal traction boundary condition (B.C.2).

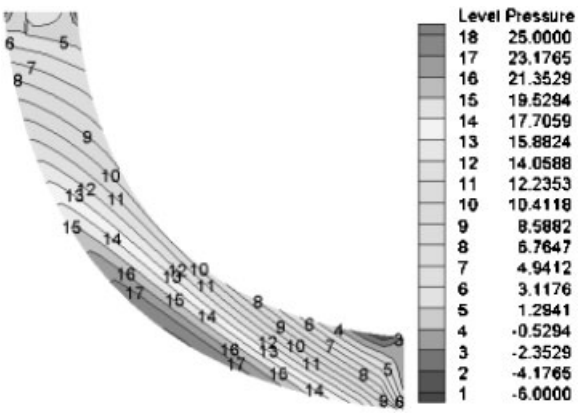

Figure 18. Contour plot of pressure over the vertical central plane using body force only boundary condition (B.C.3).

6.4. Computational time

During computation, the computational time has been recorded for three periods. The first period is from the beginning to end of the evaluation of all boundary and domain integrals in Equations (14) and (21). To ensure computational accuracy and save computational time, the adaptive integration technique [25] is employed. The number of Gauss points in the use of the Gauss quadrature is determined by the minimum distance between the source point and field point and the size of the element/cell under consideration. The second period refers to the forming of all matrices of system Equations (45)–(47). And the last period is the time spent solving the system of equations using the *modified Powell hybrid algorithm*. Table VI lists the computational time for the three examples described above in the three computational periods.

Table IV. Results at maximum velocity position of each section over the vertical central plane $y=0$ (see Figure 14) using tangential velocity and normal traction boundary condition (B.C.2).

Section	x	z	u_x	u_z	$\|u\|$	p
1	10.000	−10.250	2.0251	0.0000	2.0251	0.0000
3	8.8179	−9.8488	1.5241	−0.5572	1.6227	9.5336
5	7.7094	−9.6240	1.7535	−0.6085	1.8561	16.3958
7	6.6745	−9.3255	1.8135	−0.7952	1.9802	22.3943
9	5.7133	−8.9534	1.8158	−1.0043	2.0750	27.4799
11	4.8257	−8.5076	1.7783	−1.2283	2.1613	31.6812
13	4.0118	−7.9882	1.7062	−1.4622	2.2470	35.0681
15	3.2715	−7.3952	1.6020	−1.7009	2.3366	37.7390
17	2.6048	−6.7285	1.4691	−1.9385	2.4323	39.8117
19	2.0118	−5.9882	1.3118	−2.1698	2.5355	41.4133
21	1.4924	−5.1743	1.1360	−2.3931	2.6491	42.6663
23	1.0466	−4.2867	0.9487	−2.6102	2.7773	43.6740
25	0.6745	−3.3255	0.7582	−2.8367	2.9362	44.4831
27	0.3760	−2.2906	0.5676	−3.1257	3.1768	45.0054
29	0.1512	−1.1821	0.3241	−3.6385	3.6529	44.6710
31	0.1250	0.0000	0.0000	−2.4893	2.4893	50.0000

Table V. Results at maximum velocity position of each section over the vertical central plane $y=0$ (see Figure 14) using body force only condition (B.C.3).

Section	x	z	u_x	u_z	$\|u\|$	p
1	10.000	−10.375	1.4924	−0.6161	1.6146	−0.8171
3	8.8179	−9.8488	1.1560	−0.2889	1.1915	5.6939
5	7.7094	−9.6240	1.2718	−0.3390	1.3162	9.8961
7	6.6745	−9.3255	1.2969	−0.4812	1.3833	13.2274
9	5.7133	−8.9534	1.2880	−0.6300	1.4338	15.6751
11	4.8257	−8.5076	1.2536	−0.7838	1.4785	17.2654
13	4.0118	−7.9882	1.1959	−0.9401	1.5212	18.0464
15	3.2715	−7.3952	1.1165	−1.0951	1.5639	18.0824
17	2.6048	−6.7285	1.0176	−1.2442	1.6074	17.4490
19	2.0118	−5.9882	0.9029	−1.3828	1.6514	16.2261
21	1.4924	−5.1743	0.7767	−1.5086	1.6968	14.4896
23	1.0466	−4.2867	0.6443	−1.6196	1.7431	12.3039
25	0.6745	−3.3255	0.5114	−1.7213	1.7957	9.7078
27	0.3760	−2.2906	0.3829	−1.8300	1.8696	6.6971
29	0.1512	−1.1821	0.2437	−2.0250	2.0396	3.1584
31	0.1250	0.0000	0.0348	−1.5443	1.5447	2.1552

From the above table we can see that the distribution of computational time in three periods is different for different problems. Since the problem is density-independent in the first example (*Poiseuille flow*), the third period occupies a very small portion of the total computational time. Since there are no internal nodes in the second example (*driven cavity flow*), Equation (21) is not used and consequently the first period occupies a very small portion of the total

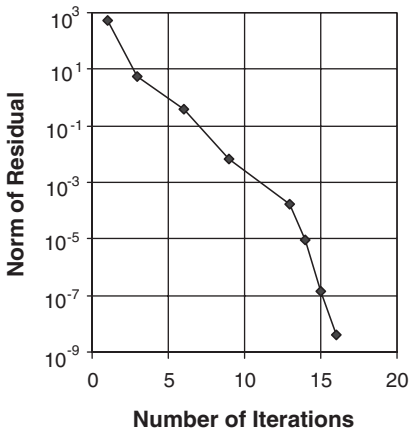

Figure 19. Iteration history for pipe flow.

Table VI. Computational time in different stages (min).

Example	Number of boundary nodes	Number of total nodes	Time for evaluation of integrals	Time for forming system	Time for solving system	Total time (min)
Poiseuille	1146	1581	18	61	15	94
Cavity	1922	1922	8	172	26	206
Pipe	719	3503	86	43	92	221

computational time. The common phenomenon in the three examples is that the second period occupies more computational time, especially in the second example. This is due to the use of the simple *Gauss–Jordan elimination* method to invert the matrix $[A]$ in Equation (48). To reduce the computational time in this period, a robust matrix inverse tool is needed.

7. CONCLUDING REMARKS

A new boundary-domain integral equation method is presented for three-dimensional viscous flow. The derived formulation is general and promising, applicable to steady, unsteady, compressible, and incompressible flows. Three numerical examples for steady incompressible flows demonstrated the correctness and potential of the method.

For internal points, the complex-variable technique is employed to compute the pressure and, therefore, no strongly singular domain integrals need to be treated. For boundary points, explicit formulation is given for computing the boundary pressure.

The distinct advantage of the derived formulation is that no velocity gradients and pressure appear in the system of equations. Therefore, the system of equations has far less unknowns than in FDM and FEM and faster iteration convergence can be achieved than in the existing BEM.

In this paper, the *Gauss–Jordan elimination* method is used to invert the boundary coefficient matrix [*A*] and the *modified Powell hybrid algorithm* is employed to solve the final system of equations. To improve the computational efficiency, more powerful tools may be used. For very complicated problems, Multi–Region technique [19, 31] should be incorporated into this method to reduce the equation size and computer storage.

REFERENCES

1. Roache PJ. *Computational Fluid Dynamics* (revised edn). Hermosa Press: Albuquerque, 1976.
2. Patankar SV. *Numerical Heat Transfer and Fluid Flow*. McGraw-Hill: New York, 1980.
3. Reddy JN, Gartling DK. *The Finite Element Method in Heat Transfer and Fluid Dynamics*. CRC Press: Boca Raton, FL, 1987.
4. Gao XW. A boundary element method without internal cells for two-dimensional and three-dimensional elastoplastic problems. *ASME Journal of Applied Mechanics* 2002; **69**:154–160.
5. Gao XW, Chen PC, Tang L. Deforming mesh for computational aeroelasticity using a nonlinear elastic boundary element method. *AIAA Journal* 2002; **40**:1512–1517.
6. Wu JC, Thompson JF. Numerical solutions of time-dependent incompressible Navier–Stokes equations using an integral-differential formulation. *Computers in Fluids* 1973; **1**:197–215.
7. Skerget P, Alujevic A, Brebbia CA. The solution of Navier–Stokes equations in terms of vorticity–velocity variables by boundary elements. *BEM VI*. Computational Mechanics Publications: Southampton, 1984.
8. Onishi K, Kuroki T, Tanaka M. An application of the boundary element method to incompressible laminar viscous flow. *Engineering Analysis* 1984; **1**:122–127.
9. Kitagawa K, Brebbia CA, Wrobel LC, Tanaka M. Boundary element analysis of viscous flow by penalty function formulation. *Engineering Analysis* 1986; **3**:194–200.
10. Grigoriev MM, Fafurin AV. A boundary element method for steady viscous fluid flow using penalty function formulation. *International Journal for Numerical Methods in Fluids* 1997; **25**:907–929.
11. Ladyzhenskaya OA. *The Mathematical Theory of Viscous Incompressible Flow*. Gordon and Breach: New York, 1963.
12. Bush MB, Tanner RI. Numerical solution of viscous flows using integral equation method. *International Journal for Numerical Methods in Fluids* 1983; **3**:71–92.
13. Aydin M, Fenner RT. Boundary element analysis of driven cavity flow for low and moderate Reynolds numbers. *International Journal for Numerical Methods in Fluids* 2001; **37**:45–64.
14. Tosaka N, Onishi K. Boundary integral equations formulations for steady Navier–Stokes equations using the Stokes fundamental solution. *Engineering Analysis with Boundary Elements* 1985; **2**:128–132.
15. Tosaka N, Fukushima N. Integral equation analysis of laminar natural convection problems. *BEM VIII*. Computational Mechanics Publications: Southampton, Springer: Berlin, 1986.
16. Power H, Partridge PW. The use of Stokes' fundamental solution for the boundary only formulation of the three-dimensional Navier–Stokes equations for moderate Reynolds numbers. *International Journal for Numerical Methods in Engineering* 1994; **37**:1825–1840.
17. Nardini D, Brebbia CA. A new approach for free vibration analysis using boundary elements. In *Boundary Element Methods in Engineering*, Brebbia CA (ed.). Springer: Berlin, 1982; 312–326.
18. Sarler B, Kuhn G. Primitive variable dual reciprocity boundary element method solution of incompressible Navier–Stokes equations. *Engineering Analysis with Boundary Elements* 1999; **23**:443–455.
19. Power H, Mingo R. The DRM subdomain decomposition approach to solve the two-dimensional Navier–Stokes system of equations. *Engineering Analysis with Boundary Elements* 2000; **24**:107–119.
20. Florez WF, Power H, Chejne F. Multi-domain dual reciprocity BEM approach for the Navier–Stokes system of equations. *Communications in Numerical Methods in Engineering* 2000; **16**:671–681.
21. Dargush GF, Banerjee PK. A boundary element method for steady incompressible thermoviscous flow. *International Journal for Numerical Methods in Engineering* 1991; **31**:1605–1626.
22. Banerjee PK, Honkala KA. Development of BEM for thermoviscous flow. *Computer Methods in Applied Mechanics and Engineering* 1998; **151**:43–62.
23. Gao XW. A boundary-domain integral equation method in viscous fluid flow. *International Journal for Numerical Methods in Fluids* 2004; **45**:463–484.
24. Liepmann HW, Roshko A. *Elements of Gasdynamics*. Dover Publications: New York, 2001.
25. Gao XW, Davies TG. *Boundary Element Programming in Mechanics*. Cambridge University Press: Cambridge, 2002.
26. Gao XW, Liu DD, Chen PC. Internal stresses in inelastic BEM using complex-variable differentiation. *Computational Mechanics* 2002; **28**:40–46.

27. More JB, Hillstrom K. User guide for MINPACK-1. *Argonne National Labs Report ANL80-74*, Argonne, IL, 1980 (program HYBRJ can be downloaded from: http://netlib.org/minpack/).
28. Granger RA. *Fluid Mechanics*. Dover Publications: New York, 1995.
29. Ghia U, Ghia KN, Shin CT. High-Re solutions for incompressible flow using the Navier–Stokes equations and a multigrid method. *Journal of Computational Physics* 1982; **48**:387–411.
30. Skerget L, Hribersek M, Kuhn G. Computational fluid dynamics by boundary-domain integral method. *International Journal for Numerical Methods in Engineering* 1999; **46**:1291–1311.
31. Gao XW, Davies TG. 3D multi-region BEM with corners and edges. *International Journal of Solids and Structures* 2000; **37**:1549–1560.

